Numerical Model and Optimization of the Soil Temperature Profiles in the Context of Climatic Variability in Côte D'Ivoire

Sahi Roland Diomande*, Yao N'Guessan, and Kotchi Remi N'Guessan

Department of Mechanics, Energy and Materials Science, Felix Houphouet-Boigny National Polytechnic Institute, Yamoussoukro, Côte d'Ivoire

* Corresponding author: Tel: +225-0757373053; email: roland.diomande19@inphb.ci (S.R.D.)
Manuscript submitted July 29, 2024; revised August 21, 2024; accepted September 9, 2024; published February 17, 2025.
doi: 10.17706/ijapm.2025.15.1.13-34

Abstract: Climate change affects ambient temperature through exchanges between the components of the soil-plant-atmosphere system. This impacts thermal comfort inside buildings, leading to heavy dependence on mechanical air conditioning. To mitigate the regulated thermal effects of the interaction of the above-mentioned system, planting trees in cities remains one of the decisive solutions. The aim of this article is to set up a numerical simulation and optimization model of soil temperature profiles in the city of Yamoussoukro (Côte d'Ivoire) under two conditions (bare surface and covered surface) to assess the impact that changes in the temperature inside the soil have on the ambient temperature. The simulation took solar energy as the natural source of heat, producing a temperature gradient at the undisturbed soil profiles. The energy source was calculated by acquiring meteorological data over two years (2017–2018), with a time step of one minute. The finite element method was used to discretize the heat equation in space, and the finite difference method was used to discretize it in time. The resulting ordinary differential equation was numerically simulated using the 4th-order Runge-Kutta method. Particle Swarm Optimization was used to find optimal temperature profiles that would have no effect on the ambiance. The equations were implemented in MATLAB R2021b software. The model was validated by measuring soil and air temperatures and relative humidity in real-life situations over two seasons using a laboratory-built data acquisition instrument. The results showed that the presence of plants in a city reduces the ambient temperature, and the predicted values agree with the measured data. In a city, when the average annual temperature of the first 20 cm of soil depth exceeds 20 °C, tree planting becomes imperative.

Keywords: Numerical simulation, soil temperature, climate variability, finite element method, Particle Swarm Optimization (PSO)

1. Introduction

Soil temperature is an important meteorological property that strongly influences its chemical, thermophysical (thermal conductivity, thermal diffusivity), mineralogical, mechanical and biological properties [1]. Soil temperature has a feedback effect on ambient thermophysical properties. To this end, knowledge of the temperature profiles within soils is of interest to several fields of application, such as agriculture, geothermal energy, solar energy, environmental management [2], and civil engineering. This soil temperature controls the thermo-hydric equilibrium that is established between the soil surface [3] and the atmosphere, as well as the physical processes involved [4].

In the thermo-hydric equilibrium processes between the temperature of the subsurface soil layers (0–40 cm) and the ambient temperature [5], prior knowledge of the variation in soil temperature is decisive for taking ecological measures (reforestation, construction of ecological buildings, etc.) and combating global warming. These ecological actions will enable people to reduce their high demand for mechanical air conditioning in buildings and maintain their health. The focus of the present study is on the impact on ambient temperature of variations in the temperature of the soil with or without trees in a city.

A number of studies have been carried out to determine soil temperature profiles [6], using analytical models [6–9], empirical models [10–14], numerical models [15–20], neural network models [21], and experimental techniques [22]. The soil temperature profile depends not only on its own parameters [23] (mineralogy, texture, granulometry, thermal diffusivity and conductivity), but also on environmental properties (wind potential, ambient air temperature, latent heat flux, sensible heat flux, etc.) [24]. This makes its assessment a matter of careful implementation of the equations in order to opt for a more suitable solution. Although techniques for estimating soil temperature profiles do exist, they are unfortunately limited by long-term diurnal and seasonal variations. In addition, the heterogeneity of the climate in a greenhouse produces convective heat fluxes that vary from one point on the soil surface to another [25].

Changing environmental conditions put soil properties at risk. Models for estimating soil temperature range from the simple to the complex, leaving the accuracy to the complex models (despite the difficulties encountered in setting them up) [2]. Previous models have been based on modified soil profiles (soils reworked during sampling and laboratory experiments) [25]. These models were based on estimates of the various fractions of liquid, gaseous and solid phases and of the granulometry and textural compartments of the soils [26]. These quantities did not express a perfect reality, but they only gave a vision of the constitution of the soil and the phenomena that could occur in it. Determining the optimum temperature profile within the soil is an important spatio-temporal characteristic of the soil-plant-atmosphere relationship. Lateral flows of water and heat in heterogeneous porous media can lead to significant losses in thermo-hydric properties caused by evaporation [27] and transpiration from plant leaves. At the soil-atmosphere interface, water and energy fluxes are highly dynamic and influenced by variations in temperature, the moisture gradient at different horizons, and the direction of water infiltration and heat transfer [28]. These reasons limit the practices and theories of previous modeling efforts [26].

To overcome these deficiencies, we have developed a numerical approach that takes into account heat transfer in both directions [26] (upward energy flux governed by evapotranspiration and downward energy flux governed by the temperature gradient between the surface and underlying layers). The aim of this article is to establish a mathematical model for assessing the impact of vegetation cover on variations in ambient temperature and to implement a decision criterion for achieving thermal comfort. Bidirectional heat propagation and evapotranspiration using a natural heat source supplied to the soil and plants are taken into account.

Specifically, the aim is to: (i) determine the intensity of the conductive heat flux within the soil, governed by solar energy, using the closed energy balance equation; (ii) establish a mathematical model for simulating the soil temperature profile of bare and covered soil surfaces using the calculated conductive energy and study the impact of plants in a city; and (iii) establish a decision criteria based on the particle swarm optimization algorithm to find the average annual subsurface soil temperature above which the population should adopt ecological practices. The model was validated using measured data.

2. Materials and Methods

2.1. Materials

2.1.1. Study areas and database

The study was carried out in two towns in the department of Yamoussoukro (latitude: 6.828, longitude: –5.289), Côte d'Ivoire. Yamoussoukro has an average annual rainfall of 1,028 mm and a relatively flat topography. The landscape is characterized by flat lowlands and very flat, low granite mountain ranges with an average altitude of around 200 m. Ferrallitic soils are the most abundant, with vegetation consisting of mesophilous forests, gallery forests and shrubby Savannah [29]. Our study focused on moderately humified ferralitic soils with sandy-clay textures on granitic and sedimentary rocks. The climate is humid tropical [30] with two seasons: a rainy season (March to October) and a dry season (November to February) [29]. Weather data from two years (2017–2018) recorded by Vantage Pro2 brand stations was used. The parameters measured by this station are ambient temperature, relative humidity, precipitation, wind speed and direction.

2.1.2. Measuring instruments

A data acquisition system was designed and built in the laboratory to prevent soil disturbance (Fig. 1). A metal rod into which DSB28 and DHT 11 sensors are inserted and protected by polystyrene thermal insulation (apart from the sensor end outlets) prevented thermal disturbance caused by contact between the rod and the ground. The sensors measure soil temperature from –40 °C to +150 °C, with an accuracy of 1%.

Fig. 1. Data acquisition system.

2.2. Methods

2.2.1. Assessment of the heat source within the soil

Soil and plants are subjected to a heat source calculated from the energy balance [31]:

$$G(t,z) = R_n(t) - (H(t) + \lambda E(t)) \quad (1)$$

$G(t,z)$: heat conduction flux in the soil (W/m^2); $H(t)$: sensible heat flux at the soil surface (W/m^2); $\lambda E(t)$: latent heat flux to soil and plants (W/m^2); $R_n(t)$: net radiation intensity at the soil surface (W/m^2).

To calculate the components of conductive heat, we needed to know the net solar radiation heat fluxes, sensible heat fluxes and latent heat fluxes, based on our assumptions.

2.2.1.1. Assumptions

Soil temperature simulation is based on exchanges between the soil, the plants, and the atmosphere, assuming that:

- The space-time characteristics of a layer of soil and ambient air measured at the same altitude at the same time are identical.

- Heat exchanges take place horizontally by convection in the air, vertically by conduction in the soil, by radiation and by evapotranspiration at the soil surface.
- Plants in the same plot have the same average canopy height, leaf resistance and leaf temperature; the entire soil surface has a constant rate of plant cover.

2.2.1.2. Assessment of the energy fluxes

The intensity of net solar radiation ($R_n(t)$) is expressed by Stefan-Boltzmann's law [32]:

$$R_n(t) = (1-\alpha) \cdot R_{swd}\,(t) + \varepsilon \cdot \sigma \left(\varepsilon_a \cdot \left(U_{k=10}^{n-1}\right)^4 - \left(U_{k\in[0,5]}^{n-1}\right)^4\right) \tag{2}$$

α : albedo of the earth's surface; ε: ground surface emissivity; σ: Stefan-Boltzmann constant; ε_a: effective emissivity of the atmosphere; $U_{k=10}^{n-1}$: air temperature measured at a height of 10 m (°C); $U_{k\in[0,5]}^{n-1}$: soil surface temperature (°C), measured between 0 and 5 cm into the ground; $R_{swd}(t)$: downward solar radiation.

The sensible heat flux $\left(H(t)\right)$ under wet environmental conditions is given by [5]:

$$H(t) = (1-\Lambda)\left(R_n(t) - G_0(t)\right) \tag{3}$$

Λ : actual evaporation fraction; $G_0(t)$: global solar irradiation (W/m^2)

The Surface Energy Balance System (SEBS) model is used to calculate the evapotranspiration fraction [33]:

$$\begin{cases} \Lambda = \Lambda_r . \lambda \dfrac{E_{wet}(t)}{R_n(t)-G_0(t)} & (a) \\ \Lambda_r = 1 - \dfrac{H(t)-H_{wet}(t)}{H_{dry}(t)-H_{wet}(t)} & (b) \end{cases} \tag{4}$$

with, $$\begin{cases} H_{wet}(t) = \dfrac{(R_n(t)-G_0(t)) - \dfrac{\rho_{air}.c_{P,air}}{r_a + r_{leaves} + r_{soil}} \dfrac{e_s.e_a}{\gamma}}{\left(1+\frac{\Delta}{\gamma}\right)} \\ \lambda E_{wet}(t) = R_n(t) - G_0(t) - H_{wet}(t) \\ H_{dry}(t) = R_n(t) - G_0(t) \end{cases}$$

r_{leaves}: stomatal resistance of leaves (s/m); r_{soil}: resistance to water vapor diffusion in the soil (s/m); $H_{dry}(t)$: sensible heat in dry conditions; E_{wet}: evaporation from the soil surface; $H_{wet}(t)$: sensible heat in wet conditions$C_{P,air}$; = 1.012 J/kg: specific heat of air; ρ_{air} : air density; e_a: air vapor pressure measured at the reference surface (2 m); e_s: air vapor pressure at saturation; r_a: aerodynamic resistance measured at the reference surface (2 m); γ: psychrometric constant; Δ: saturation vapor pressure gradient at ambient temperature.

The sensible heat equation in its final form is:

$$H(t) = \frac{\left(H_{dry}(t)-H_{wet}(t)\right)\left(R_n(t)-G_0(t)\right) - H_{dry}(t).\lambda E_{wet}(t)}{\left(H_{dry}(t)-H_{wet}(t)-\lambda E_{wet}(t)\right)} \tag{5}$$

The parameters of this formula were calculated from meteorological data that had been sequenced into two typical seasons (a dry season for clear-sky days and a wet season for rainy days).

The latent heat flux (λE) is assessed by [34] :

$$\lambda E\,(t) = \Lambda.\left(R_n(t) - G_0(t)\right) \tag{6}$$

2.2.2. Numerical simulation and optimization of the soil temperature

The heat equation was numerically solved to predict the mean soil temperature profile based on meteorological data. The finite element method was used for the appropriate numerical discretization of this equation.

2.2.2.1. Heat equation, functional spaces and boundary conditions

The heat migration in the soil is governed by numerically solving the heat equation in a domain $\Omega = [z_{min}, z_{max}]$ in time $t \in [0, T]$ [5]:

$$\begin{cases} \frac{\partial u}{\partial t}(z,t) + min_{i=1,\dots,m}\left[-D\left(\frac{\partial^2 u}{\partial z^2}(z,t) + (\alpha + \beta)_{\partial\Omega_0}\right) - G(t,z)\right] = 0, \text{ in } [0,T] X\, \Omega \quad (a) \\ u(z, t=0) = u_0(z) \quad on\ [0,T] X\, \Omega \quad (b) \\ \frac{\partial u}{\partial \eta}(z=0,t) = \alpha \quad on\ [0,T]\, X\, \partial\Omega_0 \quad (c_1) \\ \frac{\partial u}{\partial \eta}(z = z_{max}, t) = \beta \quad on\ [0,T]\, X\, \partial\Omega_0 \quad (c_2) \\ \frac{\partial u}{\partial \eta}(z,t) = 0 \quad on\ [0,T]\, X\, \partial\Omega \quad (d) \end{cases} \tag{7}$$

$D = D(z,t)$: soil thermal diffusivity (m^2/s) considered constant because its values are little affected by temperature variation [35]; (a): heat equation; (b) : initial conditions; (c_1), (c_2) and (d): boundary conditions of Eq. (7a) ; $\alpha \geq \beta > 0$, where α and β are constants and $t \in [0,T]$; $\vec{\eta}$: external, centrifugal normal vector placed at the boundary of the domain Ω.

2.2.2.2. Numerical prediction of the solution to the heat equation

We consider Ω to be a regular bounded open of $\mathbb{R}^N$ and a heat flux $G(t,z) \in L^2([0,T]; L^2(\Omega))$, with $L^2(\Omega)$ the Banach space and a regular initial data belonging to a Hilbert subspace $\left(u_0(z) \in H_0^1(\Omega)\right)$. This leads to a unique solution $u \in L^2([0,T]; H_0^1(\Omega)) \cap C\left([0,T]; L^2(\Omega)\right)$ of the heat equation [36]. The principle of the finite element method is to multiply the initial Eq. (7a) by a test function (υ) in a Sobolev space $H_0^1(\Omega)$. Any test function $\upsilon \in H^1(\Omega)$ is continuous on $H_0^1(\Omega)$ and a regular solution of the heat equation in the sense that $\frac{\partial \upsilon}{\partial z} \in L^2([0,T]; L^2(\Omega))$ [37]. The solution of the equation $u \in L^2\left([0,T]; H^2(\Omega)\right) \cap C\left([0,T]; H_0^1(\Omega)\right)$ and the test function $\upsilon \in L^2([0,T]; H_0^1(\Omega)) \cap C\left([0,T]; L^2(\Omega)\right)$ have been obtained. The Sobolev space is a subspace of the Hilbert space $H^1(\Omega)$ defined by:

$$H^1(\Omega) = \left\{ v \in L^2(\Omega), such\ that, \forall\, i \in \{1,\dots,N\}, \frac{\partial v}{\partial z_i} \in L^2(\Omega), partial\ derivative\ in\ the\ weak\ sense \right\} \tag{8}$$

To make it easier to solve the equation, we first omit the various boundary conditions, to which we will return later. The heat equation becomes:

$$\frac{\partial u}{\partial t}(z,t)v(z) + min_{i=1,\dots,m}\left[-D\left(\frac{\partial^2 u}{\partial z^2}(z,t)v(z) + \left(\alpha(t) + \beta(t)\right)_{\partial\Omega_0} v(z)\right) - G(t,z)v(z)\right] = 0, \quad in\ [0,T] X\Omega \tag{9}$$

By applying Green's Theorem, we can perform integration by parts [37] in the Ω domain. This gives an equivalent equation of the type:

$$\int_\Omega \frac{\partial u}{\partial t}(z,t)v(z)dz + min_{i=1,2,\dots,m}\left[-D\left(-\int_\Omega \frac{\partial u}{\partial z}(z,t)\frac{\partial v}{\partial z}(z)dz + \int_{\partial\Omega}\frac{\partial u}{\partial z}(z,t)v(z).\vec{\eta}\,.\overrightarrow{dS} - (\alpha + \beta)(t)\int_{\partial\Omega_0} v(z)\,dz\right) - \int_\Omega G(t,z)\,v(z)dz\right] = 0, \quad in\ [0,T]\, X\, \Omega \tag{10}$$

Taking into account only the Dirichlet's condition on the adiabatic sidewalls, all values of the test function (v) at the boundary of the $\partial\Omega$ domain cancel. This gives a new equation:

$$\int_\Omega \frac{\partial u}{\partial t}(z,t)v(z)dz + min_{i=1,2,\dots,m}\left[D\left(\int_\Omega \frac{\partial u}{\partial z}(z,t)\frac{\partial v}{\partial z}(z)dz - (\alpha + \beta)(t)\int_{\partial\Omega_0} v(z)\,dz\right) - \int_\Omega G(t,z)\,v(z)dz\right] = 0, \quad in\ [0,T]\, X\, \Omega \tag{11}$$

The $u(t,z)$ solution of the heat Eq. (11) and its natural heat source $G(t,z)$ are functions of time t, taking their values in the Ω domain space. Eq. (11) is written:

$$\int_{\Omega|z} \frac{\partial u}{\partial t}(z,t)dt \int_{\Omega|t} v(z)dz + min_{i=1,2,\dots,m}\left[D\left(\int_{\Omega} \frac{\partial u}{\partial z}(z,t).\frac{\partial v}{\partial z}(z)dz - (\alpha+\beta)(t)\int_{\partial\Omega_0} v(z)\,dz\right) - \int_{\Omega} G(t,z)\,v(z)dz\right] = 0, \quad in\ [0,T]\,X\,\Omega \tag{12}$$

Since the domain Ω and the test function $v_h(z)$ are time invariant, we write:

$$\frac{d}{dt}\int_{\Omega} \frac{\partial u}{\partial t}(z,t)dt \int_{\Omega} v(z)dz + min_{i=1,2,\dots,m}\left[D\left(\int_{\Omega} \frac{\partial u}{\partial z}(z,t).\frac{\partial v}{\partial z}(z)dz - (\alpha+\beta)(t)\int_{\partial\Omega_0} v(z)\,dz\right) - \int_{\Omega} G(t,z)\,v(z)dz\right] = 0, \quad in\ [0,T]\,X\,\Omega \tag{13}$$

Solving the heat equation in the n-dimensional Hilbert space $(V_h\,\epsilon H^1(\Omega))$ is done by a variational approximation in its subspace $V_{0h}\ \epsilon\ H_0^1(\Omega)$ to obtain n-equations with n unknowns.

The finite element space is based on the discrete space of globally continuous functions on each mesh. This space is defined by:

$$V_{0h} = \{v \in V_h, \quad such\ that \quad v(0) = v(1) = 0\} \tag{14}$$

According to the Compactness Theorem, we note [38]:

- $\prec u_k{}^1(t), v \succ$, is the scalar product of $\int_{\Omega} \frac{\partial u}{\partial t}(z,t)dt \int_{\Omega} v(z)dz$;
- $\prec (\alpha(t), \beta(t)), v \succ_{\partial\Omega_0}$, the scalar product of $(\alpha(t)+\beta(t)).\int_{\partial\Omega_0} v(z)\,dz$;
- $a(u_k(t), v) = \int_{\Omega} \frac{\partial u}{\partial z}(z,t).\frac{\partial v}{\partial z}(z)\,dz$, is a continuous bilinear form of $H_{0h}^1(\Omega)$ for $v\,\epsilon\,V_{0h}$ (V_{0h} being a subspace of the Hilbert space).
- $\prec G(t), v \succ$ is the scalar product of $\int_{\Omega} G(t,z).v(z)dz$, which is a continuous linear form of $H^1(\Omega)\ \epsilon\ L^2(\Omega)$.

By choosing the test function in the $H_0^1(\Omega)$ space of the variational formulation, the heat equation takes the form of an ordinary differential equation with boundary conditions that are easier to solve. We obtain the internal variational formulation, which consists of finding $u(t)$, a function of $[0,T]$ with values in $H_0^1(\Omega)$ of resolution:

$$\begin{cases} \frac{d}{dt} \prec u_k(t), v \succ + min_{i=1,2,\dots,m}\left[D\left(a(u_k(t),v) - \prec (\alpha(t),\beta(t))_{\partial\Omega_0}, v \succ_{\partial\Omega_0}\right) - \prec G_k(t), v \succ_{L^2(\Omega)}\right] = 0, & \\ \qquad \forall\, v\,\epsilon\,H_0^1(\Omega), \ in\ [0,T]\,X\,\Omega & (a) \\ u_k(t=0) = u_{0,h}(z) \qquad on\ [0,T]\,X\Omega & (b) \\ \frac{\partial u_0}{\partial \eta}(t) = \alpha \qquad on\ [0,T]X\partial\Omega_0 & (c_1) \\ \frac{\partial u_{k=ndl}}{\partial \eta}(t) = \beta \qquad on\ [0,T]X\partial\Omega_0 & (c_2) \\ \frac{\partial u_k}{\partial \eta}(t) = 0 \qquad on\ [0,T]\,X\partial\Omega & (d) \end{cases} \tag{15}$$

with $V_{0h} = H_0^1(\Omega)$.

According to the Lax-Milgram Theorem, the relation (2.15-(a)) admits a unique solution $u_k(t)$ (existence and uniqueness of the solution) [38]. Moreover, $u_0 \in H_0^1(\Omega)$ is an approximation of the initial solution $u_0(z)$ at the upper boundary, whose validity comes from the Trace Theorem [39]. The fact that $u_0 \in L^2(\Omega)$,($L^2(\Omega)$ being a Banach space) [37] where L^2 is a Hilbert space and $G_k \in L^2([0,\mathrm{T}]\,;\ H_0^1(\Omega)) \cap C([0,T];\ L^2(\Omega))$ then the set of components of the heat equation admits a unique solution $u_k(t) \in L^2([0,\mathrm{T}]\,;\ H_0^1(\Omega)) \cap C([0,T];\ L^2(\Omega))$.

According to the discrete minimum principle [40], the variational annotation of Eq. (15a) in the weak sense is given:

---

[1] k explains the spatial points for calculating the thermal profiles within the soil according to depth

$$\left(\frac{\partial u_k}{\partial t}(t), v - u_k(t)\right) + D\left[a\left(u_k(t), v - u_k(t)\right) - \prec \left(\alpha(t), \beta(t)\right), v - u_k(t) \succ_{\partial\Omega_0}\right] \leq \prec G_k(t), v - u_k(t) \succ_{L^2(\Omega)}, \quad \forall\ v \in H_0^1(\Omega),$$
$$in\quad [0, T]\ X\ \Omega \tag{16}$$

To solve this system, we introduce a 'hat function' $(\emptyset_k)_{1 \leq k \leq ndl}$ of $H_0^1(\Omega)$ in the finite element basis, and we pose $v_h = (\emptyset_k)_{1 \leq k \leq ndl}$, with ndl, the degree of freedom. Consider U_k, a vector in $\mathbb{R}^{ndl}$ with coordinates of u_1, so that the decomposition of u_k on the basis of $\emptyset_k$ is written as $u_k = \sum_{k=1}^{ndl} u_k . \emptyset_k$ and we pose:

$$U_k = \sum_{k=1}^{ndl} u_k(z) = (u_1, u_2, \dots, u_{ndl}), \quad \forall\ t \in [0, T] \tag{17}$$

For a regular mesh, when $\emptyset_k(z_i)$ to $\emptyset_k(z)$, $0 \leq i, k \leq ndl$, we define the 'hat' function by:

$$\emptyset_k(z) = \emptyset\left(\frac{z_i - z_k}{h}\right) = \begin{cases} 1 & if \quad i = k \\ 0 & otherwise \end{cases} \tag{18}$$

The spatial pitch is defined by $h = z_{k+1} - z_k$. Through the values of h at the mesh nodes, the basis function allows any function of V_{0h} to be unisolvantly characterized [22]. For any function $u_k \in V_{0h}$ uniquely defined by its values at the nodes $(z_k)_{1 \leq k \leq ndl}$ in the space $V_{0h} \in H_0^1(\Omega)$ of dimension n, the function $u_k \in V_{0h}$ is defined by:

$$u_k(z) = \sum_{k=1}^{ndl} u_k(z_k)\emptyset_k(z) \approx \sum_{k=1}^{ndl} u_k(z_k)\emptyset_k, \quad \forall\ z_k \in \Omega \tag{19}$$

The heat Eq. (16) becomes:

$$\frac{d}{dt}\sum_{k=1}^{ndl} u_k(z_k)\int_\Omega \emptyset_k . \emptyset_i\, dz + D\sum_{k=1}^{ndl} u_k(z_k)\int_\Omega \emptyset_k \emptyset_i\, dz - D(\alpha(t) + \beta(t))\int_{\partial\Omega} \emptyset_k \emptyset_i dz \leq \int_\Omega G(t)\emptyset_i\, dz, \qquad \forall\ v \in V_h,\ in\ [0, T] \tag{20}$$

In the Compact notation, the Eq. (20) is written as:

$$\frac{d}{dt} \prec u_k . \emptyset_k, \emptyset_i \succ + D.a\left(\sum_{k=1}^{ndl} u_k . \emptyset_k, \emptyset_i\right) - D. \prec \left(\alpha(t), \beta(t)\right). \emptyset_k, \emptyset_i \succ_{\partial\Omega_0} \leq \dots \prec G(t), \emptyset_i \succ_{L^2(\Omega)},$$

$$\forall\ \emptyset_i \in V_{0h}, 1 \leq i, k \leq ndl,\ in\ [0, T]\ X\ \Omega \tag{21}$$

The last approach consisted of using the finite element method for spatial discretization, and the finite difference method for temporal discretization, since the implementation of a finite element method in space and time is of no particular interest when the domain Ω is invariant in time [37].

2.2.2.3. Semi-discretization in space

The weak variational formulation of the heat equation is discretized in space. In this discretization, the spatial step is written as an index. To do this, an internal variational approximation is established by introducing a finite-dimensional subspace $V_{0h} \in H_0^1(\Omega)$. Typically, V_{0h} is a finite element subspace Q_k, for a uniform rectangular mesh. The semi-discretization of the Eq. (21) is the variational approximation in the weak sense:

Find $u_h(t)$ as a function of [0, T] with values in V_{0h} such that:

$$\frac{d}{dt} \prec u_{k,h}(t). \phi_k, \phi_i \succ_{L^2(\Omega)} + Da\left(\sum_{k=1}^{ndl} u_{k,h}(t). \phi_k, \phi_i\right) \leq \prec G(t), \emptyset_i \succ_{L^2(\Omega)} + D \prec \left(\alpha(t), \beta(t)\right)\emptyset_k, \emptyset_i \succ_{\partial\Omega_0}, \quad \forall\ \phi_i \in V_{0,h},\ 1 \leq i, k \leq ndl,\ in\ [0, T] X\ \Omega \tag{22}$$

Introducing a basis $(\emptyset_k)_{1 \leq k \leq ndl}$ of the finite elements of V_{0h}, we look for $u_h(t)$ in the form:

$$u_h(t) = \sum_{k=1}^{ndl} U_{k,h}(t). \emptyset_k \tag{23}$$

with $U_h = \left(U_{k,h}\right)_{1 \leq k \leq ndl}$: coordinate vector of $u_{k,h}$.

The ϕ_k functions are independent of time, unlike the coordinates of $U_{k,h}(t)$. We note $\alpha = \sum_{k=1}^{ndl} U_{0,h}(t).\emptyset_k$ and $\beta = \sum_{k=1}^{ndl} U_{k=ndl,h}(t).\emptyset_k$, i.e., $\alpha(t) = \sum_{k=1}^{ndl} \alpha_{k=0}(t)$ and $\beta(t) = \sum_{k=1}^{ndl} \beta_{k=ndl}(t)$.

For $1 \leq i, k \leq ndl$, the heat equation and its boundary conditions are written:

$$\begin{cases} \sum_{k=1}^{ndl} \prec \phi_k, \phi_i \succ_{L^2(\Omega)} \frac{dU_{k,h}(t)}{dt} + D \sum_{k=1}^{ndl} a(\phi_k, \phi_i)\, U_{k,h}(t) \leq \prec G(t), \emptyset_i \succ_{L^2(\Omega)} + D \prec (\alpha(t), \beta(t))\emptyset_k, \emptyset_i \succ_{\partial\Omega_0}, \\ \qquad \forall\ \phi_i \in V_{0,h},\ 1 \leq i,k \leq ndl,\ \ in\ [0,T]\ X\ \Omega \quad (a) \\ U_{k,h}(z, t=0) = U_{0,h}(z), \qquad \forall\ U_{0,h}(z) \in V_{0,h},\ \ on\ \ [0,T]\ X\Omega \quad (b) \\ \frac{\partial U_{k=0,h}}{\partial \eta}(z=0,t) = \alpha \qquad on\ \ [0,T]X\partial\Omega_0 \ \ (c_1) \\ \frac{\partial U_{k=ndl,h}}{\partial \eta}(z=z_{max},t) = \beta \qquad on\ \ [0,T]X\partial\Omega_0 \ \ (c_2) \\ \frac{\partial U_{1\leq k<ndl,h}}{\partial \eta}(z,t) = 0 \qquad on\ \ [0,T]X\ \partial\Omega \quad (d) \end{cases} \tag{24}$$

The established equations are implemented by defining the mass matrix and the stiffness matrix. The 'mass matrix' $M_{i,k,h}$ is defined by [41]:

$$M_{i,k,h} = \prec \phi_k, \phi_i \succ_{L^2(\Omega)} \tag{25}$$

The coefficients of the 'mass matrix' are evaluated using the following structure [5]:

$$M_{i,k,h} = \begin{cases} \frac{2}{3}h & for \quad k = i \\ \frac{1}{6}h & if \quad |k-i| = 1 \\ 0 & otherwise \end{cases} \tag{26}$$

We also define the 'stiffness matrix' $K_{i,k,h}$:

$$K_{i,k,h} = \int_\Omega \phi_k'.\phi_i' dz = a(\phi_k, \phi_i) \tag{27}$$

The coefficients of this stiffness matrix are calculated as follows:

$$K_{i,k,h} = \begin{cases} \frac{2}{h} & \text{for} \quad k = i \\ \frac{-1}{h} & if \quad |k-i| = 1 \\ 0 & otherwise \end{cases} \tag{28}$$

The heat equation approximation is equivalent to a system of ordinary differential equations given by:

$$\begin{cases} M_{i,k,h}.\frac{d\,U_{k,h}}{dt}(t) + D.K_{i,k,h}.U_{k,h}(t) \leq G_i(t) + D.K_{i,k,h}.(\alpha+\beta)(t)\,, \quad \forall\, 1 \leq i,k \leq ndl,\ \ in\ [0,\mathrm{T}]\ X\ \Omega \ \ (a) \\ U_{k,h}(z, t=0) = U_{0,h}(z) \qquad \forall\ U_{0,h}(z) \in V_{0,h},\ \ on \quad [0,T]X\Omega \quad (b) \\ \frac{\partial U_{k=0,h}}{\partial \eta}(z=0,t) = \alpha \qquad on\ \ [0,T]X\partial\Omega_0 \quad (c_1) \\ \frac{\partial U_{k=ndl,h}}{\partial \eta}(z=z_{max},t) = \beta \qquad on\ \ [0,T]X\partial\Omega_0 \quad (c_2) \\ \frac{\partial U_{1\leq k<ndl,h}}{\partial \eta}(z,t) = 0 \qquad \text{on} \quad [0,T]\ X\ \partial\Omega \quad (d) \end{cases} \tag{29}$$

2.2.2.4. Time discretization

The finite difference method is used to discretize the differential Eq. (29) in time. The system of equations is rewritten as:

$$\begin{cases} M_{i,k,h}\frac{dU_{k,h}^n}{dt} + DK_{i,k}U_{k,h}^n \leq \ G_i^n + D.K_{i,k,h}\,(\alpha+\beta)^n, \quad \forall \ \ 1 \leq i,k \leq ndl,\ \ in\ [0,\mathrm{T}]\ X\ \Omega \quad (a) \\ U_{k,h}(z, t=0) = U_{0,h}^0\,, \qquad \forall\ U_{0,h}^0 \in V_{0,h}\,,\ \ on\ \ [0,T]X\Omega \qquad (b) \\ \frac{\partial U_{k=0,h}}{\partial \eta}(z=0,t) = \ \alpha^n \qquad on\ \ [0,T]X\partial\Omega_0 \quad (c_1) \\ \frac{\partial U_{k=ndl,h}}{\partial \eta}(z=z_{max},t) = \ \beta^n \qquad on\ \ [0,T]X\partial\Omega_0 \ \ (c_2) \\ \frac{\partial U_{1\leq k<ndl,h}}{\partial \eta}(z,t) = 0 \qquad on \quad [0,T]X\ \partial\Omega \ \ (d) \end{cases} \tag{30}$$

For an infinitesimal variation in the time interval ($\Delta t = dt$), we break $[0, T]$ down into N_n sub-intervals. Each sub-interval Δt corresponds to the 'time step' which measures the length of time between two successive instants t_n. and and t_{n-1}. This length is defined by $\Delta t = \frac{T-t_0}{N_n}$ where N_n corresponds to the number of node iteration points such that $N_n = ndl$ for $t_n = t_{n-1} + \Delta t$ and $t_{n-1} = n.\Delta t$, with $0 \leq n \leq N_h$. We denote $U_{k,h}^{n-1}$, the approximation of $U_{k,h}(t_{n-1})$ at time t_{n-1}, and $U_{k,h}^{n}$, the approximation of $U_{k,h}(t_n)$ at time t_n, used for the rest of the numerical scheme.

In practical implementation, time is meshed on the basis of the day in minutes ($t_{n-1} = 24 \times 60$), and spatial meshing is performed every 2.5 cm ($z_{n-1} = 2.5 \times 100$).

2.2.2.5. Total spatial-temporal discretization

The numerical solution of the studied system of equations is obtained using the θ-scheme. In practice, this scheme is unconditionally stable for $\theta \in [\frac{1}{2}, 1]$. The space-time discretization of the heat Eq. (30a) is obtained:

$$\begin{cases} M_{i,k,h}.\frac{U_{k,h}^{n}-U_{k,h}^{n-1}}{\Delta t} + D.K_{i,k,h}.\left[\theta.U_{k,h}^{n} + (1-\theta).U_{k,h}^{n-1} - \theta.\alpha^{n} - (1-\theta).\alpha^{n-1} - \theta.\beta^{n} - (1-\theta).\beta^{n-1}\right] \leq \theta.G_i^n + (1-\theta).G_i^{n-1}, \\ \qquad \forall \ 1 \leq i,k \leq ndl, \quad in\ [0,\mathrm{T}]\ X\ \Omega \qquad (a) \\ U_{k,h}^{n}(z, t=0) = U_{0,h}^{0} \qquad \forall\ U_{0,h}^{0} \in V_{0,h},\quad on\ [0,T]X\Omega \quad (b) \\ \frac{\partial U_{k=ndl,h}(z_k=z_0,t)}{\partial \eta} = D.K_{i,k,h}(\theta\alpha^{n} + (1-\theta)\alpha^{n-1}) \qquad on\ [0,T]X\ \partial\Omega_0 \quad (c_1) \\ \frac{\partial U_{k=ndl,h}(z_k=z_{max},t)}{\partial \eta} = D.K_{i,k,h}(\theta\beta^{n} + (1-\theta)\beta^{n-1}) \qquad on\ [0,T]\ X\ \partial\Omega_0 \quad (c_2) \\ \frac{\partial U_{1\leq k<ndl,h}(z_k,t)}{\partial \eta} = 0 \qquad on\ [0,T]\ X\ \partial\Omega \quad (d) \end{cases} \tag{31}$$

with $U_k^n = \sum_{i=1}^{ndl} U_i^n$ and $U_k^{n-1} = \sum_{i=1}^{ndl} U_i^{n-1}$.

The temperature propagation in the ground is considered as a one-dimensional and anisotropic evolution in a heterogeneous medium.

2.2.2.6. Choice of method and numerical solution of the ordinary differential equation

In order to obtain an accurate numerical solution of the Ordinary Differential Equation, the Runge-Kutta method of order 4 is chosen because [42] it automatically updates the calculated values.

Let be the estimates $U_{k-1,h}^{n-1}$, $U_{k,h}^{n-1}$, $U_{k+1,h}^{n-1}$ and $U_{k,h}^{n}$ at times t_{n-1}, t_n established at spatial nodes $k-1$, k, $k+1$ in the domain Ω meshed in h. Eq. (31) is assumed to be a Cauchy problem and is given Neumann conditions in each phase. This problem is written as follows:

$$\begin{cases} U_{k,h}^{n} \leq U_{k,h}^{n-1} + {M_{i,k,h}}^{-1}.\Delta t\left[(\theta\, G_i^n + (1-\theta)G_i^{n-1}) - DK_{i,k,h}\left(\theta U_{k,h}^{n} + (1-\theta)U_{k,h}^{n-1} - (\theta.\alpha^{n}(1-\theta).\alpha^{n-1} - \theta.\beta^{n} - (1-\theta).\beta^{n-1})\right)\right], \\ \qquad \forall \ 1 \leq i,k \leq ndl, \quad in\ [0,\mathrm{T}]\ X\ \Omega \quad (a) \\ U_{k,h}^{n}(z, t=0) = U_{0,h}^{0} \qquad \forall\ U_{0,h}^{0} \in V_{0,h},\quad on\ [0,T]X\Omega \quad (b) \\ \frac{\partial U_{k=ndl,h}(z_k=z_0,t)}{\partial \eta} = K_{i,k,h}.D.[\theta\alpha^{n} + (1-\theta)\alpha^{n-1}] \qquad on\ [0,T]X\ \partial\Omega_0 \quad (c_1) \\ \frac{\partial U_{k=ndl,h}(z_k=z_{max},t)}{\partial \eta} = K_{i,k,h}.D.[\theta\beta^{n} + (1-\theta)\beta^{n-1}] \qquad on\ [0,T]\ X\ \partial\Omega_0 \quad (c_2) \\ \frac{\partial U_{1\leq k<ndl,h}(z_k,t)}{\partial \eta} = 0 \qquad on\ [0,T]\ X\ \partial\Omega \quad (d) \end{cases} \tag{32}$$

2.2.2.7. Conditions for obtaining the numerical solution of the non-linear temperature profile

The term $U_{k,h}^{n}$, on the right-hand side of the ordinary differential inequality Eq. (32a) is approximated by $V_{k,h}^{n}$ to obtain the non-linear soil temperature profile. We therefore evaluated $V_{k,h}^{n}$ by the left-handed decentralized one-step explicit Euler method. For $V_{k,h}^{n} = U_{k,h}^{n}$, we have:

$$V_{k,h}^{n} = U_{k,h}^{n-1} + \frac{D.\Delta t}{h^2}\left(U_{k-1,h}^{n-1} - 2U_{k,h}^{n-1} + U_{k+1,h}^{n-1}\right) \tag{33}$$

After rearrangement, we obtain the expression for $V_{k,h}^{n}$:

$$V_{k,h}^{n} = \left(1 - 2\frac{D.\Delta t}{h^2}\right).U_{k,h}^{n-1} + \frac{D.\Delta t}{h^2}.(U_{k+1,h}^{n-1} + U_{k-1,h}^{n-1}) \tag{34}$$

Because of the numerical stability of the θ-scheme, we take $\theta = {}^{1}/_{2}$ because the explicit Euler method is unconditionally stable and the CFL (Courant-Friedrich-Levy) condition in ∞ is satisfied $(2.D.\Delta t.U_{k,h}^{n-1} \leq h^2)$ [43]. Eq. (32a) is rewritten as:

$$U_{k,h}^{n} \leq U_{k,h}^{n-1} + {M_{i,k,h}}^{-1}.\Delta t.\left[\theta G_i^n + (1-\theta)G_i^{n-1} - DK_{i,k,h}\left(\theta.V_{k,h}^{n} + (1-\theta)U_{k,h}^{n-1} - (\theta\,\alpha^n + (1-\theta)\alpha^{n-1} + \theta\beta^n + (1-\theta)\beta^{n-1})\right)\right],\ \forall\ 1 \leq i,k \leq ndl,\quad in\ [0,\mathrm{T}]\ X\ \Omega \tag{35}$$

By replacing $V_{k,h}^{n}$ with its expression in Eq. (32a), we obtain:

$$U_{k,h}^{n} \leq U_{k,h}^{n-1} + {M_{i,k,h}}^{-1}.\Delta t\left[\left(\theta\, G_i^n + (1-\theta)G_i^{n-1}\right) - DK_{i,k,h}\left[\theta\left(\left(1-2\frac{D.\Delta t}{h^2}\right).U_{k,h}^{n-1} + \frac{D.\Delta t}{h^2}(U_{k+1,h}^{n-1} + U_{k-1,h}^{n-1})\right) + (1-\theta).U_{k,h}^{n-1} - (\theta\alpha^n + (1-\theta)\alpha^{n-1} + \theta.\beta^n + (1-\theta)\beta^{n-1})\right]\right],\quad \forall\ 1 \leq i,k \leq ndl,\quad in\ [0,\mathrm{T}]\ X\ \Omega \tag{36}$$

With $\alpha_{av} = \sum_{k=1}^{ndl}\alpha_{k=0}(t) = \theta\alpha^n + (1-\theta)\alpha^{n-1}$ and $\beta_{av} = \sum_{k=1}^{ndl}\beta_{k=ndl}(t) = \theta\beta^n + (1-\theta)\cdot\beta^{n-1}$.
Then:

$$U_{k,h}^{n} \leq U_{k,h}^{n-1} + {M_{i,k,h}}^{-1}\cdot\Delta t\left[\theta G_i^n + (1-\theta)G_i^{n-1} - DK_{i,k,h}\left[\theta\left(\left(1-2\frac{D.\Delta t}{h^2}\right)U_{k,h}^{n-1} + \frac{D\cdot\Delta t}{h^2}(U_{k+1,h}^{n-1} + U_{k-1,h}^{n-1})\right) + (1-\theta)U_{k,h}^{n-1} - (\alpha_{av} + \beta_{av})\right]\right],\quad \forall\ 1 \leq i,k \leq ndl,\quad in\ [0,\mathrm{T}]\ X\ \Omega \tag{37}$$

The Eq. (37) is expressed as:

$$U_{k,h}^{n} \leq U_{k,h}^{n-1} + \Delta t.{M_{i,k,h}}^{-1}\cdot f^{n-1},\ \forall\ \ 1 \leq i,k \leq ndl,\quad in\ [0,\mathrm{T}]\ X\ \Omega \tag{38}$$

with, $U_{k,h}^{n} = U_{k,h}(t_n)$; $U_{k,h}^{n-1} = U_{k,h}(t_{n-1})$ and $f^{n-1} = f\left(t_{n-1},\ U_{k,h}(t_{n-1})\right)$.

The temperature profile over time is obtained by integrating the function f^{n-1} over time:

$$\int_0^T f^{n-1}dt = \theta G_i^n + (1-\theta)G_i^{n-1} - DK_{i,k,h}\left[\theta\left(\left(1-2\frac{D.\Delta t}{h^2}\right)U_{k,h}^{n-1} + \frac{D\Delta t}{h^2}(U_{k+1,h}^{n-1} + U_{k-1,h}^{n-1})\right) + (1-\theta)U_{k,h}^{n-1} - (\alpha_{av} + \beta_{av})\right],\forall\ 1 \leq i,k \leq ndl,\quad in\ [0,\mathrm{T}]\ X\ \Omega \tag{39}$$

with, $n = 1,2,\ldots,N_n$.

The 4th-order Runge-Kutta method was used to increase the accuracy of the model. For details of this method, see [44].

2.2.2.8. Presentation of initial and boundary conditions

Measured mean temperatures and moisture and calculated heat flux at the soil surface and at –100 cm soil depth were used as upper surface initial conditions and lower boundary conditions, respectively. These values are uniform for all soil depths z_k at time t = 0 and are denoted $U_{0,h}^{0}$, α and β. The initial conditions for which the values of the temperature and energy fluxes do not cancel out $\left(U_{0,h}^{0}, U_{ndl,h}^{0}\right) \in \partial\Omega_0$ and $\left(G_{0,h}^{0}, G_{ndl,h}^{0}\right) \in \partial\Omega_0)$, are called "Neumann conditions". Applying the $\theta -$ scheme to the ODE, we take the mean ambient temperature and heat fluxes calculated at the soil surface and at 100 cm depth. These correspond to initial conditions and domain boundaries. On the other hand, the lateral edges, for which the flows are zero, are considered adiabatic and are referred to as Dirichlet conditions (Table 1).

Table 1. Measured values of thermal diffusivity and boundaries conditions

Soil parameters \ **Surface types**		**Covered soil**	**Bare soil**
Soil thermal diffusivity $D(z,t)$		$2.05\times10^{-6}\ (m^2/s)$	
Boundaries conditions	Measured soil temperatures	Ground surface temperature (°C)	
		26.69	30.12
		Ground temperature measured at 100 cm depth (°C)	
		17.5	18
	Heat fluxes	α at ground surface (W/m²)	
		16.19	25.54
		β at 100 cm depth (W/m²)	
		6.57	8.178

2.2.3. Optimization of the temperature profile

Optimization is used to find the best solution from many feasible solutions [37]. Feasible solutions are those that satisfy all the constraints of the optimization problem. In this case, the best solution was to minimize the soil temperature profile in order to find the optimum soil temperature that would not increase the ambient temperature [45]. The optimized function is called the objective function. The variables in this function are decision variables.

2.2.3.1. Optimum temperature equation

The Eq. (38) is rewritten as:

$$U_{k,h}^{n} - U_{k,h}^{n-1} + \Delta t M_{i,k}{}^{-1}\, min\ F_{k,h}^{n-1} \le 0, \qquad \forall\ \ 1 \le i,k \le ndl,\quad in\ [0,\mathrm{T}]\ X\ \Omega,\quad in\ [0,\mathrm{T}]\ X\ \Omega \tag{40}$$

From Eqs. (31a) and (39a), we identify the following form of equation:

$$M_{i,k,h}\frac{U_{k,h}^{n}-U_{k,h}^{n-1}}{\Delta t} = -\nabla F_{k,h}^{n-1} \tag{41}$$

The primitive of the function $\nabla F_{k,h}^{n-1}$ corresponds to the objective function below:

$$F_{k,h}^{n-1} = \left(\theta.G_i^{n} + (1-\theta).G_i^{n-1}\right)U_{k,h}^{n-1} + D.K_{i,k,h}(\alpha_{av}+\beta_{av})U_{k,h}^{n-1} - \frac{1}{2}DK_{i,k,h}\left[\theta\left(\left(1-2\frac{D.\Delta t}{h^2}\right)U_{k,h}^{n-1\,2} + \frac{D.\Delta t}{h^2}\left(\left(U_{k+1,h}^{n-1}\right)^2+\left(U_{k-1,h}^{n-1}\right)^2\right)\right) + (1-\theta)\left(U_{k,h}^{n-1}\right)^2\right],\quad \forall\ t\in[0,T]\ X\ \Omega \tag{42}$$

Minimizing this function means solving the problem:

$$U_{k,h}^{n} = U_{k,h}^{n-1} + \Delta t M_{i,k,h}{}^{-1} min\left[\left(\theta.G_i^{n} + (1-\theta)G_i^{n-1}\right)U_{k,h}^{n-1} - DK_{i,k,h}(\alpha_{av}+\beta_{av})U_{k,h}^{n-1} - \frac{1}{2}.D.K_{i,k,h}.\left[\theta\left(\left(1-2\frac{D.\Delta t}{h^2}\right)\left(U_{k,h}^{n-1}\right)^2 + \frac{D.\Delta t}{h^2}\left(\left(U_{k+1,h}^{n-1}\right)^2+\left(U_{k-1,h}^{n-1}\right)^2\right)\right) + (1-\theta)\left(U_{k,h}^{n-1}\right)^2\right]\right],\quad \forall\ \phi_i\in V_{0,h},\ \ 1\le i,k\le ndl\ in\ [0,T]\ X\ \Omega \tag{43}$$

Solving the system of Eq. (43) corresponds to a constrained multi-objective optimization:

$$\begin{cases} f_j\left(t,U_h(t,z)\right) = U_{k,h}^{n-1} + \Delta t.M_{i,k,h}{}^{-1}.min\left(F_{k,h}^{n-1}\right),\forall\ 1\le i,k\le ndl,\quad in\ [0,\mathrm{T}]\ X\ \Omega & (a) \\ \text{Constraints to:} & \\ \sum_{i=1}^{n} t(i) = T & (b) \\ \sum_{j=1}^{n} z(j) = z_{max} & (c) \\ 0\le t(i)\le T & (d) \\ 0\le z(j)\le z_{max} & (e) \end{cases} \tag{44}$$

2.2.3.2. Particle Swarm Optimization (PSO)

Metaheuristic optimization techniques reduce the shortcomings of mathematical optimization methods [46]. Genetic Algorithm (GA) and Particle Swarm Optimization (PSO) are two more attractive and popular methods for solving scientific and engineering problems [47–49]. A cross-comparison of the advantages in terms of convergence and accuracy shows that these two methods are remarkably accurate. While the genetic algorithm has a slight advantage, particle swarm optimization has a lower computational load [50]. The PSO method is an efficient algorithm developed by Kennedy and Eberhart in 1995 [34] to find the optimal solution to problems involving non-linear and non-convex ordinary differential equations [51–53]. In classical optimization problems with uniform meshes, as the number of iterations increases, the approximate solution can deviate considerably from the exact solution. For this reason, it is sometimes difficult to propose numerical methods for solving problems with initial conditions and boundary conditions [52, 53]. Therefore, this study established a model composed of finite element and finite difference methods to solve the partial differential equation and obtain an ordinary differential equation. The latter was solved by the Runge-Kutta method of order 4. The PSO method was applied to increase the convergence of its iterations and the accuracy of its optimal solution. Its formulation and coding are described in more detail in [54].

2.2.3.3. Validation of the proposed model and implementation

2.2.3.3.1. Measuring soil and ambient air temperature and humidity

The acquisition system tube was inserted into the soil to measure instantaneous variations in soil temperature and humidity at different soil depths. DHT11 sensors were used to measure ambient air temperature and relative humidity. These data were used as boundary conditions (upper and lower).

Measurements were carried out from January 1, 2017, to December 31, 2018, in the city of Yamoussoukro under two different conditions. The choice of sites was based on the criterion of having measured temperatures and humidities on a bare ground surface (built-up habitats only) and a covered ground surface (habitats with the presence of trees).

Data recording began three days after the sensors were inserted in the soil (time for stabilization of the thermo-hydric properties between the soil and the sensors). The thermal diffusivity of soils is a property whose variation is practically constant [35]. Data recording began three days after the sensors were inserted in the soil (time for stabilization of the thermo-hydric properties between the soil and the sensors) (Fig. 2). The thermal diffusivity of soils is a property whose variation is practically constant.

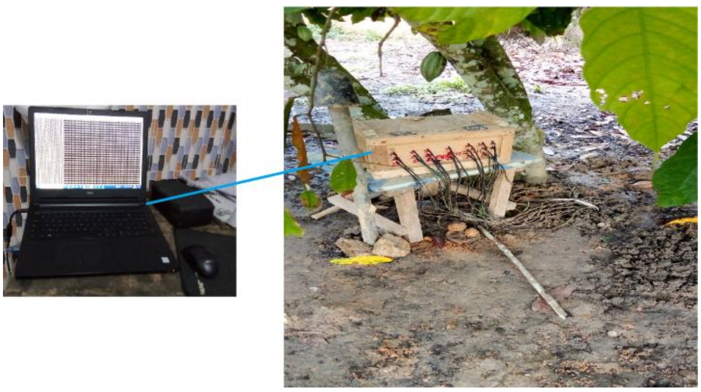

(a)

(b)

Fig. 2. Soil and ambient air temperature and humidity measurements: (a) Data acquisition; (b) Measurement of the thermal properties.

2.2.3.3.2. Statistical analysis of model performance

The performance of the proposed model is studied by estimating statistical parameters. Firstly, the Root Mean Squared Error (RMSE) between the simulated values and the measured data is calculated [20]:

$$\mathrm{RMSE} = \frac{1}{N+1}\sqrt{\sum_{i=1}^{N+1}\left(U_{pr,i,k} - U_{ob,i,k}\right)^2} \tag{45}$$

$N+1$ total number of measurements; $U_{pr,i,k}$: soil temperature predicted at time $i^{ème}$ and $k^{ème}$ depth; $U_{ob,i,k}$: soil temperature measured at time $i^{ème}$ and $k^{ème}$ depth.

The Mean Relative Error (ERM) was calculated using the Neural Network method, considering 60% of the data for the test phase, 20% for training and 20% for validation. The entire prediction model, decision criteria and model performance parameters were implemented using MATLAB R2021b software.

3. Results and Discussion

3.1. Results

3.1.1. Assessment of the soil's energy fluxes

Fig. 3 shows the variation in thermo-hydric phenomena in the soil-plant-atmosphere system that affect energy migration in the soil (heat flux by conduction, latent heat flux, sensitive heat flux, and heat flux by net solar radiation). According to this figure, the values of net radiation heat flux vary between 200 W/m^2 and 255 W/m^2; sensible heat flux varies between 100 W/m^2 and 310 W/m^2; latent heat flux varies between 0 and 150 W/m^2, and heat flux by conduction varies between –100 W/m^2 and 50 W/m^2. In addition, the intensities of net solar radiation and latent heat are greater than those of sensitive heat flux and heat flux by conduction (the lowest) in the soil. While the variation in heat by conduction is in line with that of sensitive heat, these two profiles move in opposite directions to those of latent heat and net solar radiation. It should also be noted that the intensity of latent heat remains lower than that of net solar radiation, although this is not always the case.

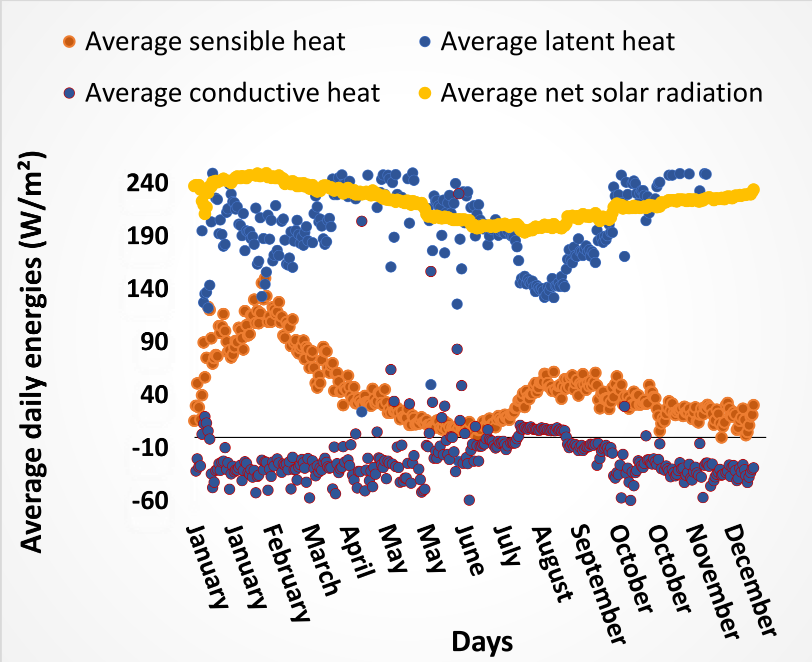

Fig. 3. Daily variations in heat fluxes.

3.1.2. Simulated temperature profiles of bare and covered soil surfaces and impact of plants in a city

3.1.2.1. Predicted temperature profiles of bare and covered soil surfaces

Fig. 4 shows the space-time variation in mean temperature profiles within the soil (Fig. 4(a) for a bare surface; Fig. 4(b) for a covered soil surface). The analysis shows that soil temperature varies significantly in the first soil layers (0 to 40 cm deep). While soil temperatures decrease from 32.83 °C and 22 °C (Fig. 5(a)) and 25.62 °C to 21.64 °C (Fig. 4(b)) in the 40 cm thick subsurface strata, these temperatures remain practically constant below a depth of 60 cm.

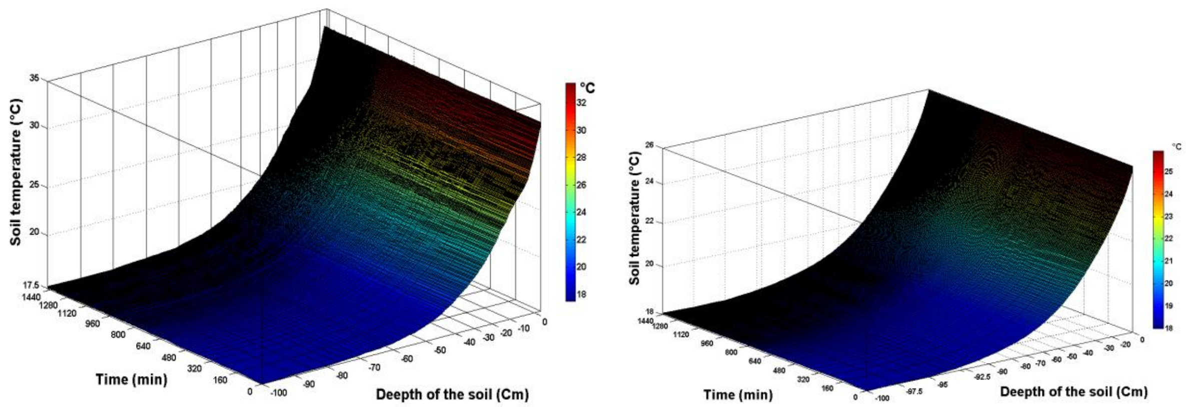

(a) (b)

Fig. 4. Space-time variation of soil temperature profile in the Yamoussoukro area: (a) bare surface ($U^0_{0,h} = 30.12°C$; $U^0_{ndl,h} = 18°C$; $\alpha = 25.54\ W/m^2$; $\beta = 8.178\ W/m^2$); (b) covered surface ($U^0_{0,h} = 26.69°C$; $U^0_{ndl,h} = 17.5°C$; $\alpha = 16.19\ W/m^2$; $\beta = 6.57\ W/m^2$).

3.1.2.2. Estimating the impact of plants in the Yamoussoukro city

Fig. 5 shows the variation in average ambient temperature measured in the town of Yamoussoukro under two conditions. The brown curve expresses the ambient temperature profile for a bare ground surface, compared with the green curve for a covered ground surface, where the difference between the two is given by the red curve. In this figure, the ambient temperatures rise rapidly from 06:20 am to reach high levels (between 30 °C and 38 °C (bare surface) and between 25 °C and 28 °C (covered surface)) during the day, before falling after 16:45 to a nighttime value of around 25 °C. The increase in temperature is less marked on vegetation-covered surfaces, whereas fairly significant increases are observed on bare ground surfaces, which increases the difference in temperature between these two surfaces. The maximum rate of increase was 27.91%, with an average of 9.37%, or 3.12 °C. Fig. 5(b) shows the variation in the relative humidity of the air around these two surfaces (blue curve for the covered surface and gray curve for the bare surface). Analysis of this figure shows that between 06:30 am and 04:45 pm, the amplitude of relative humidity is significant at the start of the day, decreasing rapidly during the day and returning to their values beyond this interval. During the study period, the covered surface had a high humidity (from 80% to 96.33% with an average of 85.57%) compared with a humidity range for the bare surface varying from 60% to 90% with an average of 72.93%.

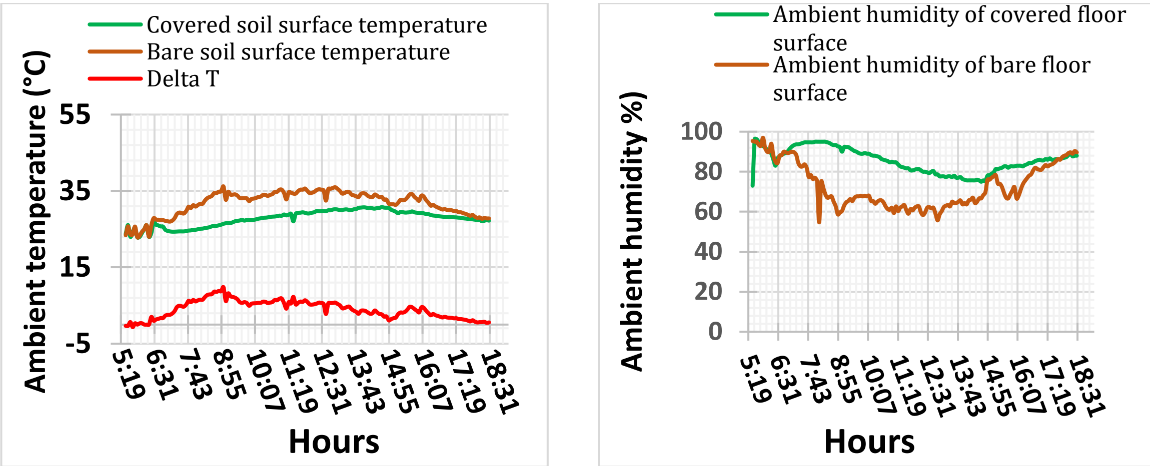

(a) (b)

Fig. 5. Effects of plants in reducing (a) ambient temperature and (b) ambient air humidity.

3.1.2.3. Optimal soil temperature profile

Optimization of the soil temperature profile showed that 20 °C is the optimum soil temperature, above which an increase in ambient temperature would have an increasing effect on the ambient air temperature. The relevance of the PSO method was shown to converge at the 5th iteration (Fig. 6).

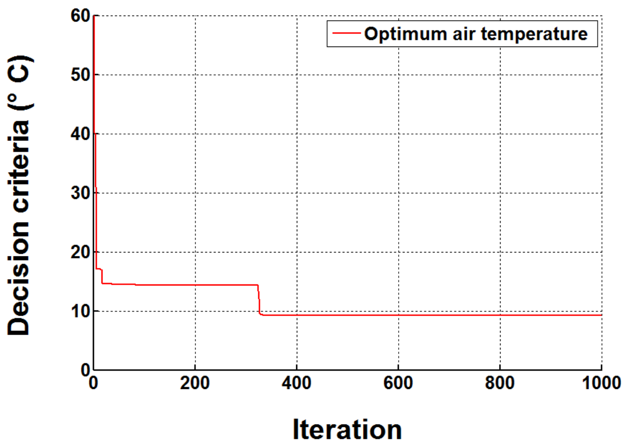

Fig. 6. Optimum floor surface temperature.

3.1.2.4. Validation of the numerical model

Prediction error analysis of the proposed model gave an MSD error equal to 3.51×10^{-5} °C, i.e., a numerical error of 35×10^{-6} (Fig. 7) and a relative error of R = 0.998. Analysis of the model's performance using the neural network method produced an error of 5.77×10^{-12}.

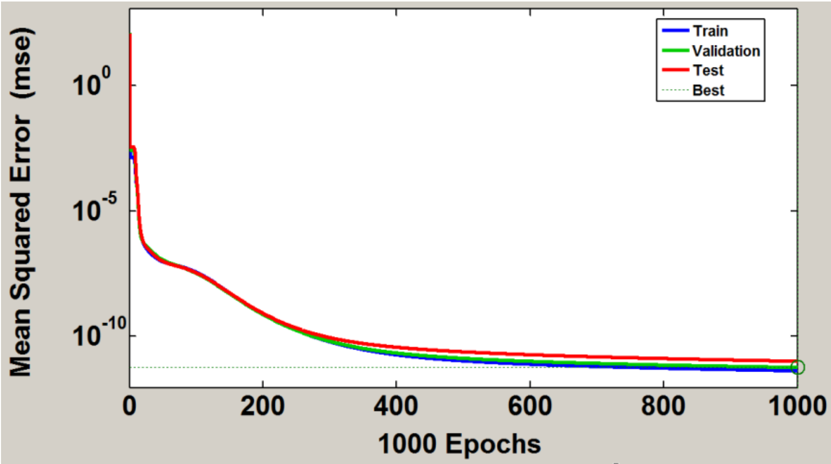

Fig. 7. Numerical model convergence profile.

3.2. Discussion

Heat and water exchange between the components of the soil-plant-atmosphere system at the earth's surface are produced by plant transpiration and evaporation from water and soil surfaces. These processes have a considerable impact on the energy balance within the soil. While latent heat explains the transpiration of plant leaves and the evaporation of water surfaces in the universe [27, 55], sensible heat explains the evaporation of soil surfaces in the atmosphere. The combination of latent heat and sensible heat results in potential evapotranspiration. The above-mentioned system operates as an open system, exchanging heat, water and matter [26] between its three components in order to achieve thermo-hydric equilibrium between them. The sun's rays are the only source of energy for this process, while rain and groundwater provide water. After some of the radiation from the earth's crust is reflected by particles suspended in the air, the plant cover and the surface of the minerals that make up the soil, the remainder, known as net solar radiation, is absorbed by the soil, increasing its conductive heat. The amount of solar radiation that penetrates the ground is greater when the ground surface is bare, and the sky is clear. The energy input by radiation is highest in the dry season and lowest in the rainy season; this contributes to the increase in latent heat and sensible heat. The conductive heat flux of the ground is the quantity of radiation gained (negative value) or lost (positive value) by it [56]. Sensible heat flux is the energy that increases atmospheric temperature, causing advection, while latent heat corresponds to the energy available for water evaporation. This justifies the strong increase in sensitive heat in the intensity of net radiation and ambient temperature in the dry seasons, compared with its low values in the rainy season [57]. In dry seasons, radiation intensity is at a maximum, so it limits the flow of water between the components of the soil-plant-atmosphere system to reduce biological phenomena (plant transpiration and microbial respiration); low values of latent heat are therefore obtained. The disadvantages of increases in ambient temperature are seen not only in the high electricity consumption in buildings [31], but also in the disruption to human health [58, 59] (strong solar radiation reflected by polluting constituents in the universe). According to the work of [60], the interaction between air temperature and soil temperature can lead to the effects of meteorological warming and climate change, thus increasing organic carbon and nitrogen emissions. On the other hand, in the rainy season, the energy input to soils and plants (important biological phenomena caused by the growth in plant height, leaf size and density, soil microorganisms, etc.) is low [59] increasing albedo. The evaporation of soil surfaces by the effects of radiant reflection in the universe, sensible heat flux and conductive heat flux are diminished compared to sensible heat flux. In addition, the intensity of latent heat remained lower than that of net solar radiation, since latent heat is a component of the radiant energy input at the Earth's surface. On the other hand, unexpected events sometimes occur because of major advection phenomena that cool the ambient air, minimizing the effects of net radiant fluxes. From one season to the next, the conductive flow is high during the day (absorption of radiant heat) and low at night (re-emission of part of the heat absorbed from the ground during the day into the atmosphere, the other part being used for the development of plants and microorganisms). In this study, average temperature increases of 9.37%, or 3.12 °C, and maximum temperature increases of 27.91%, or 10.8 °C, were obtained when moving from a covered surface (with an average relative humidity of 85.57%) to a bare surface (with an average relative humidity of 72.93%). The presence of plants increases the albedo of the soil surface. This means that planting plants in a city increases the humidity of the air and reduces the ambient temperature. This temperature increases in the morning with the intensity of net solar radiation to reach its optimum and remains constant when all the minerals in the soil and the particles suspended in the air have reached their maximum degree of thermal absorption. After 4:45 pm, this temperature decreases with the intensity of the sun's rays, so the soil particles release the heat stored during the day into the universe. Soil is a complex porous medium, composed of three phases (solid, gaseous (air) and liquid (interstitial water)) [51] represented by composite soil minerals and interstitial fluids (air and liquid). Depending on the surface texture of the minerals making up a soil, and the proportion and luster of certain minerals (quartz, feldspar, mica), the soil reflects conductive heat back into the universe; this contributes to the sensible heat flux for any increase in ambient temperature. Our results gave an average bare soil temperature of between 18 °C and 32 °C, compared with an average covered soil temperature of between 17.5 °C and 26 °C. The plant cover dampened the thermal effects of solar radiation, thus minimizing the net surface flux and hence the conductive and sensitive fluxes. Our results are similar to those of Su *et al*. [61]. The work of Rahman *et al.* [47] confirmed that an increase in the temperature inside the soil contributes significantly to an increase in the ambient air temperature and vice versa. According to the work of Raman *et al.* [53] and Lee *et al.* [62], trees, compared to grasslands, perform better in mitigating human heat stress and promote ambient temperature attenuation ranging from 3.4 °C to 2.7 °C. Sun *et al.* [63] combined the GLDAS and Noah models to analyze the evolution of soil temperature from a depth of 0-200cm. They conducted their work in China using meteorological data (1948–2018). Their results showed that strong variations in soil temperature occur from 0 to –10 cm, and that this temperature remains low at great depths (–100 cm to –200 cm). Pérez *et al*. [64] studied the impact of vegetation cover on reducing ambient temperature. Their results showed that the presence of plants on a soil reduces its ambient temperature by 0.5 °C to 5 °C and a reduction of 55% in the dry season. This increase in ambient temperature also has an impact on the temperature inside houses. Soil temperatures ranged from 0 °C to 45 °C, which are greater than those in our study, as their studies were conducted in an arid climate whereas our studies were conducted in a humid tropical climate. According to the work of Ellison *et al.* [65], forests and trees are key regulators of water, energy and carbon cycles to enhance sustainability, adaptation and mitigation efforts.

Dolschak *et al.* [66] conducted a study in Klausen-Leopoldsdorf, USA using Newton's law to predict the temperature of soil-covered surfaces and a simulator to predict the temperature of bare soil to a depth of 0 to –60 cm. The mean and absolute errors obtained were less than 0.9 °C and greater than 0.97 °C, respectively. These values are much higher than the error values in our study. Bayatvarkeshi *et al.* [67] have shown that soil temperature decreases with depth with temperatures between 0 °C and 45 °C. Contrary to our results, their results showed that the temperature was low at the beginning and end of the year. The WCANFIS model was the most efficient model for different climates. Unfortunately, this model gave an error RMSE ≈ 0.4 °C and the accuracy of their model decreased with increasing soil depth.

4. Conclusion

This study used average canopy height, leaf area, wind speed, ambient temperature, albedo, solar radiation intensity and average soil temperature measured at the surface and at 100cm soil depth to establish a mathematical model for predicting soil temperature profiles. Soil temperature was measured in a real-life situation using a soil temperature and moisture data acquisition system. The study used solar energy, calculated as a natural source of energy supplied to the soil and overlying plants.

Based on two measurement conditions (covered soil surface and bare soil surface), the results of this study showed that, not only does the increase in temperature inside the soil increase that of the ambient air and vice versa, but also, the presence of plants in a city lowers the temperatures inside the soil and the ambient air. The benefits of this practice lie in managing energy in buildings and improving human health through pleasant environmental air.

The ideal would be to have an average annual optimum temperature of 20 °C in the first 40 cm of soil. Based on the numerical prediction errors to validate the accuracy of the models, we conclude that the present model predicts temperature profiles better than the results of previous work.

The use of more than 10 years of experimental data could help future research to further increase the accuracy of the model. Secondly, it would be very interesting to compare building temperature profiles for each of these typical zones.

Use of AI tools declaration

The authors declare they have not used Artificial Intelligence (AI) tools in the creation of this article.

Conflict of Interest

All authors declare no conflicts of interest in this paper.

Author Contributions

Sahi Roland Diomande's tasks involved methodology, software, validation, formal analysis, investigation, resources, data curation, original drafting, review & editing, and visualization; Yao N'Guessan's assignments covered conceptualization, validation, resources, visualization, supervision and project administration; Kotchi Rémi N'Guessan's assignments covered conceptualization, visualization, supervision and project administration; all the authors approved the final version.

References

[1] Fathian, F., Mehdizadeh, S., Sales, A. K., & Safari, M. J. S. (2019). Hybrid models to improve the monthly river flow prediction: Integrating artificial intelligence and non-linear time series models. *J. Hydrol., 575*, 1200–1213. doi: 10.1016/j.jhydrol.2019.06.025

[2] Jaszczur, M., Polepszyc, I., Biernacka, B., & Sapińska-Śliwa, A. (2016). A numerical model for ground temperature determination. *J. Phys. Conf. Ser., 745*, 032007. doi: 10.1088/1742-6596/745/3/032007

[3] Sanikhani, H., Deo, R. C., Yaseen, Z. M., Eray, O., & Kisi, O. (2018). Non-tuned data intelligent model for soil temperature estimation: A new approach. *Geoderma, 330*, 52–64. doi: 10.1016/j.geoderma.2018.05.030

[4] Milewski, R., *et al*. (2022). Analyses of the impact of soil conditions and soil degradation on vegetation vitality and crop productivity based on airborne hyperspectral VNIR–SWIR–TIR data in a semi-arid rainfed agricultural area (Camarena, Central Spain). *Remote Sens., 14(20)*, 5131. doi: 10.3390/rs14205131

[5] Allahem, A., Boulaaras, S., Zennir, K., & Haiour, M. (2018). A new mathematical model of heat equations and its application on the agriculture soil. *Eur. J. Pure Appl. Math.*, *11(1)*, 110–137. doi: 10.29020/nybg.ejpam.v11i1.3157

[6] Holmes, T. R. H., Jackson, T. J., Reichle, R. H., & Basara, J. B. (2012). An assessment of surface soil temperature products from numerical weather prediction models using ground-based measurements: Soil temperature from numerical weather prediction models. *Water Resour. Res.*, *48(2)*. doi: 10.1029/2011WR010538

[7] Naranjo-Mendoza, C., Wright, A. J., Oyinlola, M. A., & Greenough, R. M. (2007). *A Comparison of Analytical and Numerical Model Predictions of Shallow Soil Temperature Variation with Experimental Measurements*.

[8] Droulia, F., Lykoudis, S., Tsiros, I., Alvertos, N., Akylas, E., & Garofalakis, I. (2009). Ground temperature estimations using simplified analytical and semi-empirical approaches. *Sol. Energy, 83(2)*, 211–219. doi: 10.1016/j.solener.2008.07.013

[9] Parton, W. J., & Logan, J. A. (1981). A model for diurnal variation in soil and air temperature. *Agric. Meteorol., 23*, 205–216. doi: 10.1016/0002-1571(81)90105-9

[10] Lembrechts, J. J., *et al.* (2022). Global maps of soil temperature. *Glob. Change Biol., 28(9)*, 3110–3144. doi: 10.1111/gcb.16060

[11] Carson, J. E. (1963). Analysis of soil and air temperatures by fourier techniques. *J. Geophys. Res., 68(8)*, 2217–2232. doi: 10.1029/JZ068i008p02217

[12] Costello, T. A., Braud, H. J. Jr. (1989). Thermal diffusivity of soil by nonlinear regression analysis of soil temperature data. *Trans. ASAE, 32(4)*, 1281–1286. doi: 10.13031/2013.31146

[13] Jacovides, C. P., Mihalakakou, G., Santamouris, M., & Lewis, J. O. (1996). On the ground temperature profile for passive cooling applications in buildings. *Sol. Energy, 57(3)*, 167–175. doi: 10.1016/S0038-092X(96)00072-2

[14] Kumar, R., Sachdeva, S., & Kaushik, S. C. (2007). Dynamic earth-contact building: A sustainable low-energy technology. *Build. Environ., 42(6)*, 2450–2460. doi: 10.1016/j.buildenv.2006.05.002

[15] Lequeux, J. (2019). *Fourier Heat Theory Applied to the Earth's Temperature*.

[16] Yang, C.-C., Prasher, S. O., & Mehuys, G. R. (1997). An artificial neural network to estimate soil temperature. *Can. J. Soil Sci., 77(3)*, 421–429. doi: 10.4141/S96-062

[17] Yaghoobian, N., Kleissl, J., & Krayenhoff, E. S. (2010). Modeling the thermal effects of artificial turf on the urban environment. *J. Appl. Meteorol. Climatol., 49(3)*, 332–345. doi: 10.1175/2009JAMC2198.1

[18] Tabari, H., Sabziparvar, A.-A., & Ahmadi, M. (2011). Comparison of artificial neural network and multivariate linear regression methods for estimation of daily soil temperature in an arid region. *Meteorol. Atmospheric Phys., 110(3–4)*, 135–142. doi: 10.1007/s00703-010-0110-z

[19] Mehdizadeh, S., Behmanesh, J., & Khalili, K. (2017). Evaluating the performance of artificial intelligence methods for estimation of monthly mean soil temperature without using meteorological data. *Environ. Earth Sci., 76(8)*, 325. doi: 10.1007/s12665-017-6607-8

[20] Zhang, S., Yue, Z., & Wang, T. (2018). *A 3D Thermal Model for Prediction Temperature Field During Artificial Ground Freezing*.

[21] Li, Z., Chen, J., Sugimoto, M., & Ge, H. (2019). Numerical simulation model of artificial ground freezing for tunneling under seepage flow conditions. *Tunn. Undergr. Space Technol., 92*, 103035. doi: 10.1016/j.tust.2019.103035

[22] Yilmaz, T., & Özbek, A. (2009). *Influence of Upper Layer Properties on the Ground Temperature Distribution*.

[23] Guo, H., Lin, Y., Sun, C., Mao, X., & Li, J. (2023). Effect of temperature on the dynamic parameters of silty clay in a seasonally frozen region. *Sci. Rep., 13(1)*, 13141. doi: 10.1038/s41598-023-40261-y

[24] Ferkous, K. (2021). Solar radiation characterisation and assessment for the Ghardaïa site. doi:

10.13140/RG.2.2.21780.17280 (in French)

[25] Demezhko, D. Y., & Gornostaeva, A. A. (2014). Reconstructions of long-term ground surface heat flux changes from deep-borehole temperature data. *Russ. Geol. Geophys., 55(12)*, 1471–1475. doi: 10.1016/j.rgg.2014.11.011

[26] Vanderborght, J., Fetzer, T., Mosthaf, K., Smits, K. M., & Helmig, R. (2017). Heat and water transport in soils and across the soil-atmosphere interface: 1. Theory and different model concepts. *Water Resour. Res., 53(2)*, 1057–1079. doi: 10.1002/2016WR019982

[27] Fetzer, T., Vanderborght, J., Mosthaf, K., Smits, K. M., & Helmig, R. (2017). Heat and water transport in soils and across the soil-atmosphere interface: 2. Numerical analysis. *Water Resour. Res., 53(2)*, 1080–1100. doi: 10.1002/2016WR019982

[28] Ahmadi, N., Muniruzzaman, M., Sprocati, R., Heck, K., Mosthaf, K., & Rolle, M. (2022). Coupling soil/atmosphere interactions and geochemical processes: A multiphase and multicomponent reactive transport approach. *Adv. Water Resour., 169*, 104303. doi: 10.1016/j.advwatres.2022.104303

[29] Guillaume., A., Arthur Brice, K.-W., Parfait, S. A., Hervé-Jacques, K. K., & Jea, B. (2022). Landsat 8 oli satellite imagery mapping and analysis of bedrock fracture networks in the Departments of Yamoussoukro and Toumodi (Central Cote d'Ivoire). *Eur. Sci. J. ESJ, 18(30)*, 206. doi: 10.19044/esj.2022.v18n30p206

[30] Kokobou, K. H. J., Konan-Waidhet, A. B., Soro, T. D., & Biemi, J. (2022). Mapping of potential recharge areas of fractured aquifers in the departments of Yamoussoukro and Toumodi (Central Côte d'Ivoire). *J. Geogr. Inf. Syst., 14(5)*, 527–545. doi: 10.4236/jgis.2022.145030

[31] Zhang, H., Liu, J., Li, H., Meng, X., & Ablikim, A. (2020). The impacts of soil moisture initialization on the forecasts of weather research and forecasting model: A case study in Xinjiang, China. *Water, 12(7)*, 1892. doi: 10.3390/w12071892

[32] Dambreville, R. (2014). Remote sensing forecasting of global solar radiation for the management of photovoltaic energy production. Thèse, GIPSA-lab - Grenoble Images Parole Signal Automatique, Université de Grenobl. https://theses.hal.science/tel-01130251 (in French)

[33] Su, Z. (2002). The Surface Energy Balance System (SEBS) for estimation of turbulent heat fluxes. *Hydrol. Earth Syst. Sci., 6(1)*, 85–100. doi: 10.5194/hess-6-85-2002

[34] Kennedy, J., & Eberhart, R. (1995). *Particle Swarm Optimization*.

[35] Bechkit, M. A. (2011). *On the Determination of Water Content and Infiltration Using Passive Soil Temperature Measurements*.

[36] Gordon, S. I. & Guilfoos, B. (2017). *Introduction to Modeling and Simulation with MATLAB® and Python*, 1re éd. Chapman and Hall/CRC. doi: 10.1201/9781315151748

[37] Allaire, G. (2005). Numerical analysis and optimization: An introduction to mathematical modeling and numerical simulation. Retrieved from https://books.google.ci/books?id=vReEuE4margC

[38] Almi, S., & Tasso, E. (2022). A new proof of compactness in G(S)BD. *Adv. Calc. Var.* doi: 10.1515/acv-2021-0041

[39] Lamberti, P. D., *et al*. (2019). *Provenzano, on Trace Theorems for Sobolev Spaces*.

[40] Jungel, A., & Unterreiter, A. (2005). Discrete minimum and maximum principles for finite element approximations of non-monotone elliptic equations. *Numer. Math., 99(3)*, 485–508. doi: 10.1007/s00211-004-0554-5

[41] Ferreira, A. J. M., & Fantuzzi, N. (2020). MATLAB codes for finite element analysis: Solids and structures. *Solid Mechanics and Its Applications.* Cham: Springer International Publishing. doi: 10.1007/978-3-030-47952-7

[42] Quarteroni, A., Sacco, R., Saleri, F., & Gerbeau, J.-F. (2007). *Numerical Methods: Algorithms, Analysis and*

Applications. Milan: Springer. (in French)

[43] Boulaaras, S., Hocine, M. A. B. L., & Haiour, M. (2017). L∞-error estimates of finite element methods with Euler time discretization scheme for an evolutionary HJB equations with nonlinear source terms. *J. Appl. Math. Comput. Mech., 16(1)*, 19–31. doi: 10.17512/jamcm.2017.1.02

[44] Bouameur, S. (2020). *Euler and Runge-Kutta 4th-Order Methods for 1st-Order Differential Equations*.

[45] Li, S., & Wang, X. (2021). Solving ordinary differential equations using an optimization technique based on training improved artificial neural networks. *Soft Comput., 25(5),* 3713–3723. doi: 10.1007/s00500-020-05401-w

[46] Zhong, X.-C., Chen, J.-Y., & Fan, Z.-Y. (2019). A particle swarm optimization-based method for numerically solving ordinary differential equations. *Math. Probl. Eng., 2019*, 1–11. doi: 10.1155/2019/9071236

[47] Swarup, K. S. (2006). *Swarm Intelligence Approach to the Solution of Optimal Power Flow*.

[48] Abu-Jasser, A., & Shaheen, H. (2011). *Multi-Objective Solution Based on Various Particle Swarm Optimization Techniques in Power Systems*.

[49] Liu, H., Cai, Z., & Wang, Y. (2010). Hybridizing particle swarm optimization with differential evolution for constrained numerical and engineering optimization. *Appl. Soft Comput., 10(2)*, 629–640. doi: 10.1016/j.asoc.2009.08.031

[50] Papazoglou, G., & Biskas, P. (2023). Review and comparison of genetic algorithm and particle swarm optimization in the optimal power flow problem. *Energies, 16(3)*, 1152. doi: 10.3390/en16031152

[51] Kader, M. A., Nakamura, K., Senge, M., Mojid, M. A., & Kawashima, S. (2019). Numerical simulation of water- and heat-flow regimes of mulched soil in rain-fed soybean field in central Japan. *Soil Tillage Res., 191*, 142–155. doi: 10.1016/j.still.2019.04.006

[52] Timmermans, J., Su, Z., Tol, C., Verhoef, A., & Verhoef, W. (2013). Quantifying the uncertainty in estimates of surface–atmosphere fluxes through joint evaluation of the SEBS and SCOPE models. *Hydrol. Earth Syst. Sci., 17(4)*, 1561–1573. doi: 10.5194/hess-17-1561-2013

[53] Raman, V., Kumar, M., Sharma, A., Froehlich, D., & Matzarakis A. (2021). Quantification of thermal stress abatement by trees, its dependence on morphology and wind: A case study at Patna, Bihar, India. *Urban For. Urban Green., 63*, 127213. doi: 10.1016/j.ufug.2021.127213

[54] Alam, M. N. (2016). *Particle Swarm Optimization: Algorithm and its Codes in MATLAB*. doi: 10.13140/RG.2.1.4985.3206

[55] Ariyanto, D. P., Qudsi, Z. A., Sumani, Dewi, W. S., Rahayu, & Komariah. (2021). The dynamic effect of air temperature and air humidity toward soil temperature in various lands cover at KHDTK Gunung Bromo, Karanganyar - Indonesia. *IOP Conf. Ser. Earth Environ. Sci., 724(1)*, 012003. doi: 10.1088/1755-1315/724/1/012003

[56] Moorhead, J. E. (2019). Field-scale estimation of evapotranspiration. *Advanced Evapotranspiration Methods and Applications*. doi: 10.5772/intechopen.80945

[57] Rahman, M. M., Zhang, W., & Wang, K. (2019). Assessment on surface energy imbalance and energy partitioning using ground and satellite data over a semi-arid agricultural region in north China. *Agric. Water Manag., 213*, 245–259. doi: 10.1016/j.agwat.2018.10.032

[58] Hamin, E. M., & Gurran, N. (2009). Urban form and climate change: Balancing adaptation and mitigation in the U.S. and Australia. *Habitat Int., 33(3)*, 238–245. doi: 10.1016/j.habitatint.2008.10.005

[59] Perini, K., Chokhachian, A., & Auer, T. (2018). Green streets to enhance outdoor comfort. *Nature Based Strategies for Urban and Building Sustainability* (pp. 119–129), Elsevier. doi: 10.1016/B978-0-12-812150-4.00011-2

[60] Yang, K., & Wang, J. (2008). A temperature prediction-correction method for estimating surface soil heat flux from soil temperature and moisture data. *Sci. China Ser. Earth Sci., 51(5)*, 721–729.

doi: 10.1007/s11430-008-0036-1
[61] Su, Y., *et al.* (2019). Quantifying the biophysical effects of forests on local air temperature using a novel three-layered land surface energy balance model. *Environ. Int., 132*, 105080. doi: 10.1016/j.envint.2019.105080
[62] Lee, H., Mayer, H., & Chen, L. (2016). Contribution of trees and grasslands to the mitigation of human heat stress in a residential district of Freiburg, Southwest Germany. *Landsc. Urban Plan., 148*, 37–50. doi: 10.1016/j.landurbplan.2015.12.004
[63] Sun, S., Yan, S., Cao, X., & Zhang, W. (2023). Distribution law of the initial temperature field in a railway tunnel with high rock temperature: A model test and numerical analysis. *Appl. Sci., 13(3),* 1638. doi: 10.3390/app13031638
[64] Pérez, G., Coma, J., Sol, S., & Cabeza, L. F. (2017). Green facade for energy savings in buildings: The influence of leaf area index and facade orientation on the shadow effect. *Appl. Energy, 187*, 424–437. doi: 10.1016/j.apenergy.2016.11.055
[65] Ellison, D., *et al*. (2017). Trees, forests and water: Cool insights for a hot world. *Glob. Environ. Change, 43*, 51–61. doi: 10.1016/j.gloenvcha.2017.01.002
[66] Dolschak, K., Gartner, K., & Berger, T. W. (2015). A new approach to predict soil temperature under vegetated surfaces. *Model. Earth Syst. Environ., 1(4),* 32. doi: 10.1007/s40808-015-0041-2
[67] Bayatvarkeshi, M., *et al.* (2021). Modeling soil temperature using air temperature features in diverse climatic conditions with complementary machine learning models. *Comput. Electron. Agric., 185*, 106158. doi: 10.1016/j.compag.2021.106158